



日本原子力研究開発機構機関リポジトリ  
Japan Atomic Energy Agency Institutional Repository

Title	Development of spin-contrast-variation neutron reflectometry for the structural analysis of multilayer films
Author(s)	Kumada Takayuki, Akutsu Kazuhiro, Oishi Kazuki, Morikawa Toshiaki, Kawamura Yukihiro, Sahara Masae, Suzuki Junichi, Torikai Naoya
Citation	Journal of Applied Crystallography, 52(5), p.1054-1060
Text Version	Accepted Manuscript
URL	<a href="https://jopss.jaea.go.jp/search/servlet/search?5062630">https://jopss.jaea.go.jp/search/servlet/search?5062630</a>
DOI	<a href="https://doi.org/10.1107/S1600576719010616">https://doi.org/10.1107/S1600576719010616</a>
Right	© International Union of Crystallography

## Development of spin-contrast-variation neutron reflectometry for the structural analysis of multilayer films

Authors

**Takayuki Kumada<sup>a\*</sup>, Kazuhiro Akutsu<sup>b</sup>, Kazuki Ohishi<sup>b</sup>, Toshiaki Morikawa<sup>b</sup>, Yukihiro Kawamura<sup>b</sup>, Masae Sahara<sup>b</sup>, Jun-ichi Suzuki<sup>b</sup> and Naoya Torikai<sup>c</sup>**

<sup>a</sup>Materials Sciences Research Center, Japan Atomic Energy Agency (JAEA), Tokai, Ibaraki, 319-1195, Japan

<sup>b</sup>Neutron Science and Technology Center, Comprehensive Research Organization for Science and Society (CROSS), Tokai, Ibaraki, 319-1106, Japan

<sup>c</sup>Graduate School of Engineering, Mie University, Tsu, Mie, 514-8507, Japan

Correspondence email: kumada.takayuki@jaea.go.jp

**Synopsis:** Reflectivity curves of the polarized neutrons remarkably vary as a function of proton polarization of film samples. We demonstrated that detailed structural information of each surface and interface of multilayer film samples can be obtained from these proton-polarization-dependent multiple reflectivity curves.

**Abstract:** The spin-contrast-variation neutron reflectometry technique was developed for the structural analysis of multilayer films. Polarized-neutron reflectivity curves of film samples vary as a function of their proton polarization ( $P_H$ ). The  $P_H$ -dependent reflectivity curves of a polystyrene monolayer film were precisely reproduced using a common set of structural parameters and the  $P_H$ -dependent neutron scattering length density of polystyrene. This result ensures that these curves are not deformed by inhomogeneous  $P_H$  but can be used for structural analysis. Unpolarized reflectivity curves of poly(styrene-*block*-isoprene) films were reproduced using a flat free-surface model but  $P_H$ -dependent polarized reflectivity curves were not. The global fit of the  $P_H$ -dependent multiple reflectivity curves revealed that holes with depth corresponding to one period of periodic lamellae of microphase-separated polystyrene and polyisoprene domains were produced on the surface of the films, which agrees with the microscopic results. In this manner, the spin-contrast-variation neutron reflectometry technique determines the structure of multiple surfaces and interfaces of film samples while excluding

the incorrect structure that accidentally accounts for a single unpolarized reflectivity curve only.

**Keywords:** Contrast-variation neutron reflectivity; Proton polarization; Multilayer films.

## 1. Introduction

Neutron reflectivity (NR) is used to determine the nanostructure of surfaces and interfaces of film samples based on the angle,  $\theta$ , and wavelength,  $\lambda$ , dependence of the specular reflectivity of neutron beams (Imae, 2011; Higgins & Benoît, 1996; Roe, 2000). Because of the relatively high transmittance of neutron beams, NR has an advantage over X-ray reflectivity for measuring hidden interface of multilayer films. When measuring multilayer films of soft materials, such as laminated polymers, structural information of a specific layer can be obtained by comparing the NR curve of the film with that of model samples in which hydrogen in that layer or the other layers is substituted by deuterium with much larger neutron scattering length (Crowley *et al.*, 1991*a*, 1991*b*). However, this technique can be used only when such partially deuterated model samples are prepared with exactly the same nanostructure, because even slightly different nanostructure among these samples could mislead the global analysis.

Magnetic contrast variation, which utilizes neutron magnetic scattering from a ferromagnetic reference layer beneath the film sample, has been used for the structural analysis of multilayer soft-material films (Majkrzak *et al.*, 1999; Holt *et al.*, 2009). This technique has the merit of obtaining a couple of magnetization-direction-dependent polarized NR curves from a single sample; however, it can control the scattering length density (SLD) of the ferromagnetic reference layer only but not the contrast within the film itself.

To overcome these limitations of the existing contrast variation techniques, we developed a new technique called “spin-contrast-variation neutron reflectometry (SCV-NR).” Coherent polarized-neutron scattering length of a proton,  $b_H$ , remarkably varies as a function of the proton polarization,  $P_H$ , against the neutron spin direction,

$$b_H = [-0.374 + 1.456 P_H] \times 10^{-12} \text{ (cm)}. \quad (1)$$

Thus, as  $P_H$  increases, the SLD of each layer of a multilayer film proportionally increases with the number density of protons (Fig. 1) (Knop *et al.* 1991; Sears, 1992; Brandrup *et al.*, 1999; Hartwig, 1994), resulting in the variation of NR curves. The structure of multilayer films can

be determined using the  $P_H$ -dependent NR curves from a single sample. Since Knop *et al.* (1989) first reported, the technique of spin-contrast-variation (SCV) has been used along with small-angle neutron scattering (SANS) to determine the bulk nanostructure of composite soft materials (Kohgi *et al.*, 1987; Fermon *et al.*, 1992; van den Brandt *et al.*, 2002, 2006; Kumada *et al.*, 2010; Noda *et al.*, 2011, 2016). To get started with the SCV-NR measurement, we recently developed a dynamic nuclear polarization (DNP) apparatus (Kumada *et al.*, 2018) in which proton spins in submicrometer-thick film samples are hyperpolarized by polarization transfer from unpaired electrons of doped free radicals (polarizing agents) to the protons (Abragam, 1961; Abragam & Goldman, 1978; Wenckeback, 2016).

In this study, we report the SCV-NR results of styrene homopolymer (PS) and poly(isoprene-*block*-styrene) (PSPI) film samples. The PS film was measured to confirm the homogeneity of  $P_H$ , which is essential for SCV-NR. The PSPI is so-called standard sample for the SCV-SANS measurements (Noda *et al.*, 2011). We discuss the SCV-NR results of the PSPI film based on the stock of information of the SCV-SANS study.

## 2. Experiment

### 2.1. Samples

A styrene homopolymer with weight-averaged molecular weight,  $M_w$ , of 350000 and polydispersity,  $M_w/M_n$ , of 2.1 was purchased from Aldrich (441147). PSPI with  $M_w$  in PS ( $M_{w,PS}$ ) and PI ( $M_{w,PI}$ ) blocks of 11500 and 10500, respectively, and  $M_w/M_n$  of 1.04 was purchased from Polymer Source (P1943-SIp). The PS film was prepared by spin-coating of toluene containing 2% of PS and 0.016% of 4-methacryloyloxy-2,2,6,6-tetramethylpiperidine 1-oxyl free radical (TEMPO methacrylate, Aldrich, 730297) at 5000 rpm on a 20 mm  $\times$  20 mm  $\times$  0.5 mm single-crystalline Si substrate, and then it was annealed in vacuum at 85°C for 4 days. Here, the TEMPO methacrylate is the polarizing agents for DNP. One of the two PSPI films was prepared by spin-coating of toluene containing 3.5 wt.% of PSPI and 0.035% of TEMPO methacrylate on the Si substrate at 2000 rpm, then it was annealed with the TEMPO methacrylate in nitrogen gas at 110°C, which is higher than the glass transition temperature ( $T_g$ ) of PI (-61°C) and PS (82°C) domains. The other PSPI film was prepared by spin-coating of toluene containing 2 wt.% of PSPI and 0.016% of TEMPO methacrylate on the Si substrate at 5000 rpm, annealed at 85 °C in vacuum, and then doped with TEMPO methacrylate in nitrogen gas at 60°C. Here, we name these films as strongly and weakly annealed PSPI films,

respectively.

## 2.2. Proton polarization

Protons in the PS and PSPI film samples were polarized using the DNP apparatus (Fig. S1), which consists of a cryogen-free split-pair transverse magnetic field magnet with a cryostat (Cryogenic Ltd.), a microwave, and an NMR unit (Kumada *et al.*, 2018). The protons in the film samples were dynamically polarized by irradiating 94 GHz and 600 mW microwaves from the Gunn oscillator (VCSS, GDO-10-9417F) and the amplifier (Keycom, MPA95GHz-01) at 3.36 T. The DNP conditions were precisely tuned while monitoring the NMR signal of a 20 mm × 20 mm × 0.3 mm reference sample of PS doped with TEMPO (33 mM). The temperatures of the samples were maintained at  $2.4 \pm 0.1$  K by tuning the flow rate of cold helium gas, which was recondensed by the cryocooler (Sumitomo 415D) of the magnet.

## 2.3. Neutron reflectivity measurements

The SCV-NR measurements were performed by setting the DNP apparatus into the SHARAKU polarized neutron reflectometer (BL17) of the Materials and Life Science Experimental Facility (MLF) at the Japan Proton Accelerator Research Complex (J-PARC) (Takeda *et al.*, 2012; Hayashida *et al.*, 2013). Pulsed neutrons with  $\lambda$  range of 0.24–0.88 nm and polarization higher than 99% were irradiated at  $\theta = 0.2^\circ$ – $1.5^\circ$  from the front (free-surface) side of the PS and weakly annealed PSPI films, but from the rear (Si-substrate) side of the strongly annealed PSPI film at a repetition rate of 25 Hz (Fig. S2). The spot sizes of the neutron beam on the PS, strongly annealed PSPI, and weakly annealed PSPI films were 10 mm × 10 mm, 14 mm × 14 mm, and 15 mm × 15 mm, respectively, which were maintained by adjusting slit width everytime when  $\theta$  was changed. The positively and negatively polarized SCV-NR (pSCV-NR and nSCV-NR) curves in which the neutron polarization was switched parallel and anti-parallel to the proton polarization of the film sample, respectively, were measured almost simultaneously by inverting the polarization of the incident neutrons every 30 s using the neutron spin flipper while maintaining proton polarization of the film sample. The unpolarized neutron reflectivity (UNR) curves of the proton-unpolarized films were obtained using unpolarized neutrons with a  $\lambda$  range of 0.12–0.88 nm and at  $\theta = 0.2^\circ$  and  $0.8^\circ$ . The UNR curve of the strongly annealed PSPI film was obtained after the SCV-NR measurement at room temperature, whereas the curves of the PS and weakly annealed PSPI films were obtained at the cryogenic temperature in the DNP apparatus.

### 3. Results and analysis

#### 3.1. PS film

Figure 2 compares the UNR and SCV-NR curves of the PS film as a function of the magnitude of scattering vector,  $Q$ ,

$$Q = (4\pi/\lambda) \sin \theta. \quad (2)$$

We found dissimilarity and similarity as follows: First, the nSCV-NR is higher than the UNR, and the pSCV-NR is higher than the nSCV-NR in the whole  $Q$  range. Second, the oscillation amplitude of the nSCV-NR curve is much smaller than that of the other curves, and the oscillation of the pSCV-NR curve is almost inverted as compared with that of the others. Third, the oscillation period of the pSCV-NR curve is slightly shorter than that of the UNR curve, whereas that of the nSCV-NR curve is longer than the UNR curve. Forth, the critical  $Q$ -value of the total reflection,  $Q_c$  of the pSCV-NR curve is higher than that of the others. Fifth, the slopes of these three curves are close to each other.

The solid lines represent the reflectivity curves simulated using the MOTOFIT program (Nelson, 2006) with a common set of structural parameters in Table S1, SLD of PS,  $\rho_{PS}$ , at  $P_H = 0$  and  $\pm 16\%$  in Figure 1, and the  $Q$  resolution determined by the optical layout of the reflectometer of 0.065. The UNR and SCV-NR curves, including their intensity, amplitude and phase of oscillation, total reflection, and slope, were completely reproduced by the simulation. The variation of the NR curve with  $P_H$  is qualitatively explained using the SLD profiles in the inset of Figure 2 as follows. Reflection coefficient at each surface or interface is proportional to the variation in SLD across the surface or interface; thus, its reflection intensity is proportional to the square of the difference. Among all the three profiles, the reflectivity of the pSCV-NR curve is the largest because the variation in SLD across the free surface is larger than that of the other surface and interface. The oscillation amplitude is proportional to the product of the variations in SLDs across the free surface and the PS-Si interface. The oscillation amplitude of the nSCV-NR curve is the smallest, because the variation in SLD across the free surface of the nSCV-NR is much smaller than that of the others. The oscillation is inverted in the pSCV-NR curve because  $\rho_{PS} < \rho_{Si}$  (SLD of Si) at  $P_H = 0$  and  $-16\%$ ; however,  $\rho_{PS} > \rho_{Si}$  at  $P_H = +16\%$ , i.e., the open reflection point at the interface becomes a fixed one. According to Snell's law (Roe, 2000), the angle of refracted neutrons inside the film decreases with increasing  $\rho_{PS}$ , resulting in shorter oscillation period at higher  $P_H$  (Fig. S3). When  $\rho_{PS} < \rho_{Si}$  at  $P_H = 0$  and  $-16\%$ , the total reflection occurs at the PS-Si interface and  $Q_c$  is related to  $\rho_{Si}$  (Imae,

2011),

$$Q_c = 4\sqrt{\pi\rho_{\text{Si}}}. \quad (3)$$

In contrast, when  $\rho_{\text{PS}} > \rho_{\text{Si}}$  at  $P_{\text{H}} = +16\%$ , the total reflection occurs at the free surface of the PS film and thus  $Q_c$  is related to  $\rho_{\text{PS}}$ ,

$$Q_c = 4\sqrt{\pi\rho_{\text{PS}}}. \quad (4)$$

Note that the reflectivity of the pSCV-NR curve in Figure 2 is less than 1 even at  $Q$  slightly below  $Q_c$  in Equation (4) because the film is not thick enough to block the penetration of the neutron beam.

The excellent fitting with the simulation using the uniform  $P_{\text{H}}$  of the PS film guarantees in-depth and in-plane homogeneous polarization. For example, if  $P_{\text{H}}$  near the free surface and/or the PS–Si interface were higher or lower than that inside the film, the SLD near the surface and/or interface would be higher or lower, and thus the slopes of the SCV-NR curves would deviate from the simulation accordingly. If  $P_{\text{H}}$  had serious in-plane inhomogeneity, the oscillation would be smeared, because the oscillation period varies as a function of  $P_{\text{H}}$  (Fig. S3). Therefore, we can safely determine the structure of film samples from SCV-NR curves without worrying about the deformation of the curves due to the inhomogeneity of  $P_{\text{H}}$ .

### 3.2. PSPI films

Figure 3(a) shows the UNR and SCV-NR curves of the strongly annealed PSPI film. The reflectivity of the pSCV-NR curve is much higher than that of the nSCV-NR curve at the low- $Q$  limit, but lower at  $Q > 0.07 \text{ nm}^{-1}$ . The slope of the pSCV-NR curve is remarkably steeper than that of the others. Similar to the case of the PS film, the oscillation period decreases with the increasing  $P_{\text{H}}$ . A small shoulder is observed in the pSCV-NR curve at  $Q = 0.2 \text{ nm}^{-1}$ , but not in the other curves. Figure 3(b) shows the curves of the weakly annealed PSPI film. Unlike in Figure 3(a), a Bragg peak of microphase-separated periodic lamellae of the PS and PI domains was observed at  $0.3 \text{ nm}^{-1}$ . The peak intensity increased with increasing  $P_{\text{H}}$ .

The absence of the Bragg peak in Figure 3(a) suggests that the lamellae in the strongly annealed PSPI film were disoriented during the strong annealing process. Therefore, we simulated the UNR and SCV-NR curves in Figure 3(a) using the uniform SLD,  $\rho_{\text{PSPI}}$ , in the film,

$$\rho_{\text{PSPI}} = \frac{\rho_{\text{PS}}M_{\text{w,PS}}/\delta_{\text{PS}} + \rho_{\text{PI}}M_{\text{w,PI}}/\delta_{\text{PI}}}{M_{\text{w,PS}}/\delta_{\text{PS}} + M_{\text{w,PI}}/\delta_{\text{PI}}}. \quad (5)$$

Here,  $\rho_{\text{PS}}$  and  $\rho_{\text{PI}}$  are the SLDs and  $\delta_{\text{PS}}$  and  $\delta_{\text{PI}}$  are the densities of PS and PI, respectively (Brandrup *et al.*, 1999; Hartwig, 1994). The  $P_{\text{H}} = \pm 21\%$  of the SCV-NR curves was roughly estimated from the  $P_{\text{H}}$ -dependent oscillation period (Fig. S3(b)) and precisely determined by the fitting. The simulation reproduces the UNR and SCV-NR curves except for the shoulder in the pSCV-NR curve at the  $Q$ -range between 0.07 and 0.2 nm<sup>-1</sup>. The exceptionally high reflectivity of the pSCV-NR curve at the low- $Q$  limit indicates that the curve approaches total reflection range at the PSPI–Si interface. Because  $\rho_{\text{PSPI}} > \rho_{\text{Si}}$  at  $P_{\text{H}} = +21\%$ , the total reflection of the neutron beam from the rear (Si-substrate) side of the film sample can occur at the PSPI–Si interface. The slopes of the pSCV-NR and nSCV-NR curves predominantly reflect the characteristics of the free surface and the PSPI–Si interface, respectively, because the variation in SLD across the free surface is much larger than that across the PSPI–Si interface for pSCV-NR,  $|\rho_{\text{PSPI}}| \gg |\rho_{\text{PSPI}} - \rho_{\text{Si}}|$ ; however, it is opposite for nSCV-NR,  $|\rho_{\text{PSPI}}| \ll |\rho_{\text{PSPI}} - \rho_{\text{Si}}|$ . The slope of the pSCV-NR curve is steeper than that of the nSCV-NR, indicating that the roughness of the free surface is larger than that of the interface.

What is the shoulder of the pSCV-NR curve? You may consider that the shoulder is attributed to the broadened Bragg peak of the microphase-separated periodic PS and PI lamellae, because  $Q$  of the Bragg peak in Figure 3(b) is close to that of the shoulder. However, this is not the case because the shoulder was observed neither in the UNR curve nor in the nSCV-NR curve in Figure 3(a). If the shoulder were attributed to the Bragg peak of the lamellae, as shown in Figure 3(b), the intensity would decrease with increasing  $P_{\text{H}}$ , because the difference in SLDs between PS and PI domains decreases with increasing  $P_{\text{H}}$  (Fig. 1). Instead, we simulated the curves using the hole model, which is based on the microscopic results (Fig. S4), and the reports that islands or holes with height or depth corresponding to one period of the lamellar microdomain morphology are produced on the free surface of di-block copolymer to face the lower surface energy component in vacuum (Mutter *et al.*, 1993; Hamley, 1998; Mutter & Stühn, 1995; Coulon *et al.*, 1990). Solid lines in Figure 4(a) show the simulation curves to the results in Figure 3(a) on the assumption that the strongly annealed PSPI film has 28 nm deep holes, which occupy 20% of the free surface area (Fig. S5). Using the depth close to one period of the microdomain of 20 nm, all the UNR and SCV-NR curves, including the shoulder, are successfully reproduced.

In Figure 3(b), the solid lines represent the curves of the best-fit simulation model, in which the microphase separated PS and PI lamellae are alternately and periodically stacked in parallel to the free surface and the interface, and that the PI lamellae with half thicknesses are directed

to the free surface and the interface, according to Hasegawa & Hashimoto (1985) and Liu *et al.* (2009). It is easy to reproduce the UNR curve only with this model; however, we could not find any set of structure parameters that can reproduce all of the UNR and SCV-NR curves. Even the remarkable decrease in the Bragg peak intensity of the pSCV-NR curve was not reproduced with this model. Therefore, similar to the case of the strongly annealed PSPI, we simulated the curves of the weakly annealed PSPI film using the hole model (Figure 4(b)). All of the UNR and SCV-NR curves are reproduced on the assumption that the holes occupy 40% of the free surface area.

#### 4. Discussion

It is essential for the SCV-NR technique to polarize film samples homogeneously; otherwise, we cannot safely determine structures from the SCV-NR curves. The results of Figure 2 guarantee the homogeneous polarization with our proton-polarization apparatus. DNP is sensitive to many environmental factors such as concentration of polarizing agents of TEMPO radicals and depolarizer of paramagnetic molecular oxygen impurity (Kumada *et al.*, 2009, 2012). Thus, you may consider that in-depth inhomogeneous distribution of TEMPO and molecular oxygen particularly near the surface and interface causes inhomogeneity of  $P_H$ . However, samples are homogeneously polarized due to the spin diffusion mechanism, in which the neighboring spins continually exchange energy through the energy conserving flip-flop transitions of the dipolar Hamiltonian (Abragam, 1961). van den Brandt *et al.* (2002, 2006) have shown using time-resolved SCV-SANS measurements that the gradient of  $P_H$  in nanometer length scale disappears in a few seconds. Kumada *et al.* (2010) have shown that the gradient in submicron scale disappears in a few minutes. In addition, we have demonstrated that PSPI samples were polarized almost homogeneously even when TEMPO radicals were selectively doped in their microphase-separated PS or PI domains (Noda *et al.*, 2011). The result of the homogeneous polarization of the film sample in Figure 2 is consistent with these SCV-SANS results. The coefficient of spin diffusion,  $D_{\text{spin}}$ , in soft materials is typically  $10^{-13}$  cm<sup>2</sup>/s (Abragam, 1961). The spin-lattice relaxation time,  $T_1$ , of protons in our samples is roughly 100 s around 1 K (Kumada *et al.*, 2012). Thus, the length of spin diffusion,  $l_{\text{sd}} = \sqrt{2D_{\text{spin}}T_1}$ , amounts to 40 nm, which is greater than the thicknesses of the PS and PI lamellae of the PSPI film and comparable to the general thicknesses of film samples for NR measurements. In this manner, the homogeneity of polarization in nanometer length scale is guaranteed by spin diffusion even if free radicals are more or less localized at a specific surface,

interface, or layer.

The merit of the SCV-NR measurements is to determine the structure of multiple surface and interface through the global fit of the UNR and SCV-NR curves while excluding the incorrect set of structure parameters, which accidentally reproduce the UNR curve but not the SCV-NR curve. In particular, the SCV-NR curve can selectively pick up structural information of a specific surface or interface. As mentioned above, we found the holes on the free surfaces of the strongly annealed PSPI films from the pSCV-NR curve, while the reflection from the interface was minimized.

Taking advantage of SCV-NR, we plan to measure the structure of silica coating for plastic dishes. The structural information of the silica–polymer interface is essential for the development of the coating. However, it has been difficult to obtain reflection signals from the interface in conventional reflectivity measurements because the signal from the interface is hidden by the intense reflection from the free surface of the silica coating on the polymer layer. However, the signal from the interface can be picked up by subtracting pSCV-NR from nSCV-NR of the silica–polymer bilayer film. Because the silica coating has no proton inside, the reflection from the free surface of the coating, whose intensity is independent of  $P_H$ , can be canceled out by the subtraction. In addition, reflection from the interface between polymer layer and Si substrate can be minimized by matching SLDs of the polymer and Si at moderate  $P_H$ . In this manner, the SCV-NR technique will open up new possibilities for determining the structure of multilayered films.

We have two problems in the present SCV-NR measurement. One is to simultaneously determine  $P_H$  and structure parameters from the fitting of whole SCV-NR curves. It is better to determine  $P_H$  before the fitting to decrease the number of fitting parameters for the curves. While  $P_H$  is determined from the proton-nuclear magnetic resonance (NMR) and neutron transmission in SCV-SANS measurements (Noda *et al.*, 2011), film samples for SCV-NR measurements are too thin to measure their NMR and transmission signals. The other issue is that, in many cases,  $P_H$  is not high enough to accurately determine the structure. For example, we can expect more distinct variation of the SCV-NR curves of the weakly annealed PSPI film in Figures 3(b) and 4(b) if  $|P_H|$  higher than 8% is achieved.

To overcome these problems, we are now developing a cryogen-free high-field DNP apparatus using 6.7 T magnetic field. Bornet and Jannin (2016) reported  $P_H = 91\%$  at 1.2 K and 60% at 2.2 K using their 6.7 T DNP system; therefore, we also expect such a high  $P_H$  with our new

apparatus. If only SLD of a film sample,  $\rho_f$ , exceeds  $\rho_{Si}$  at such high  $P_H$ ,  $\rho_f$  is determined from  $Q_c$  on a one-to-one basis using  $Q_c = 4\sqrt{\pi\rho_f}$  like Equation (4); thus,  $P_H$  is derived from  $\rho_f$  like Figure 1. In this manner, the SCV-NR technique will be improved for wider applications.

## 5. Conclusion

We demonstrated the SCV-NR measurements of homopolymer and di-block copolymer films whose structure has already been studied to ensure the reliability of the technique. In the first step, the in-depth and in-plane homogeneity of proton polarization was confirmed from the result that all the UNR and SCV-NR curves of the PS monolayer film was precisely reproduced using common set of structural parameters and the  $P_H$ -dependent SLD of PS. In the second step, the benefit of SCV-NR measurements was demonstrated using more complicated assembly. The SCV-NR curves of the PSPI films could not be fitted using the flat surface model, whereas the UNR curve was reproduced with this model. In contrast, all of the SCV-NR and UNR curves were reproduced using the hole model which has holes with a depth corresponding to one period of microphase-separated polystyrene and polyisoprene domains on the free surface. In this manner, while excluding the model structure that accidentally reproduces a single UNR curve only, global fits of UNR and SCV-NR curves provide structural information of multilayer films more precisely.

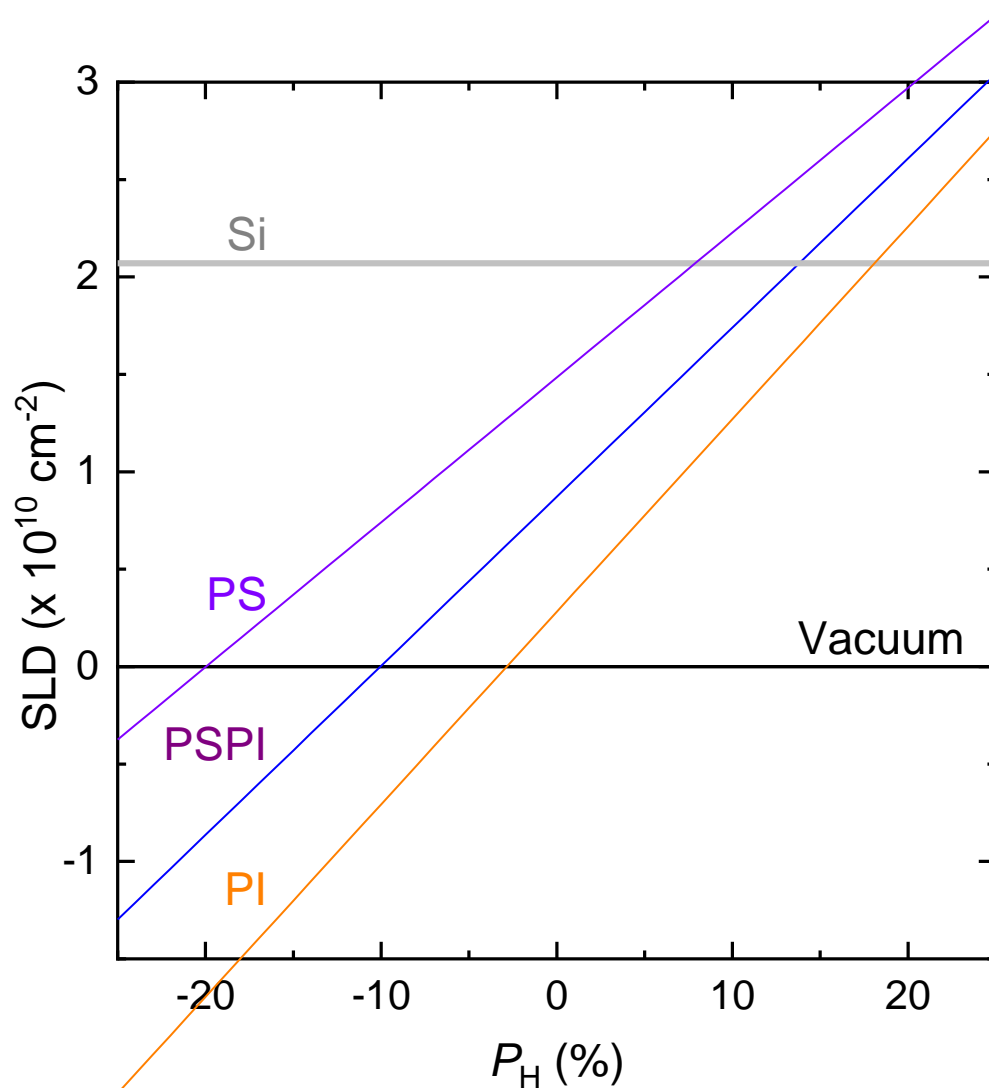


**FIGURE 1.**  $P_H$ -dependent SLDs of PS, PI, and PSPI calculated using polarized neutron scattering lengths of protons in Equation (1) and other elements (Sears, 1992); densities of PS ( $1.05 \text{ g/cm}^3$ ; Brandrup *et al.*, 1999) and PI ( $0.91 \text{ g/cm}^3$ ) at room temperature; and factor of thermal contraction (approximately 5%; Hartwig, 1994).

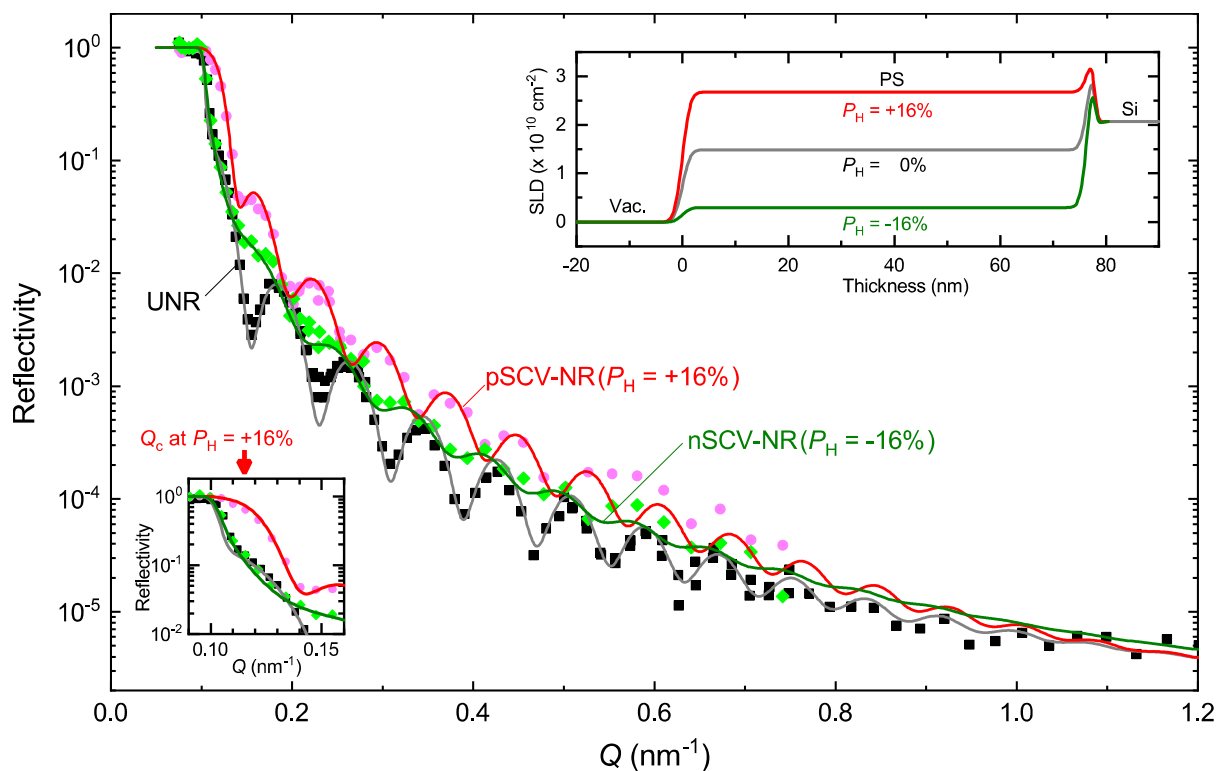


**FIGURE 2.** UNR and SCV-NR curves of the PS film. Solid lines are simulation curves using the SLD profiles in the right inset with the structure parameters in Table S1 and  $Q$  resolution of the reflectometer of 0.065. The left inset shows the enlarged NR curves near  $Q_c$ . The arrow shows  $Q_c$  obtained by substituting  $\rho_{\text{PS}}$  at  $P_H = +16\%$  in Equation (4).

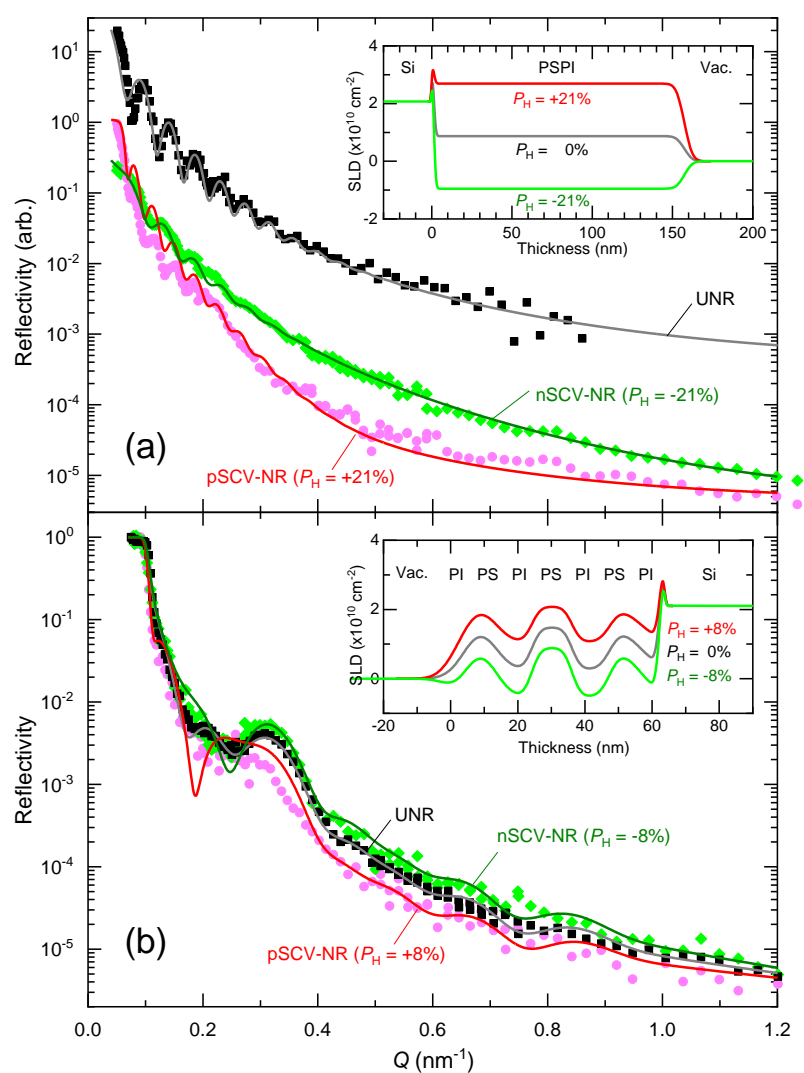


**FIGURE 3.** UNR and SCV-NR curves of the (a) strongly annealed and (b) weakly annealed PSPI films. The neutron beams were irradiated from the rear (Si-substrate) and front (free surface) side of the films in (a) and (b), respectively. Solid lines in (a) and (b) are the simulation curves using the flat surface model with the SLD profiles in the insets and the parameters in Tables S2 and S3, respectively.  $Q$  resolutions of 0.065 for the UNR curve in (a), and 0.11 for the other curves in (a) and (b) are included on the simulation. The UNR curve in (a) is offset vertically.

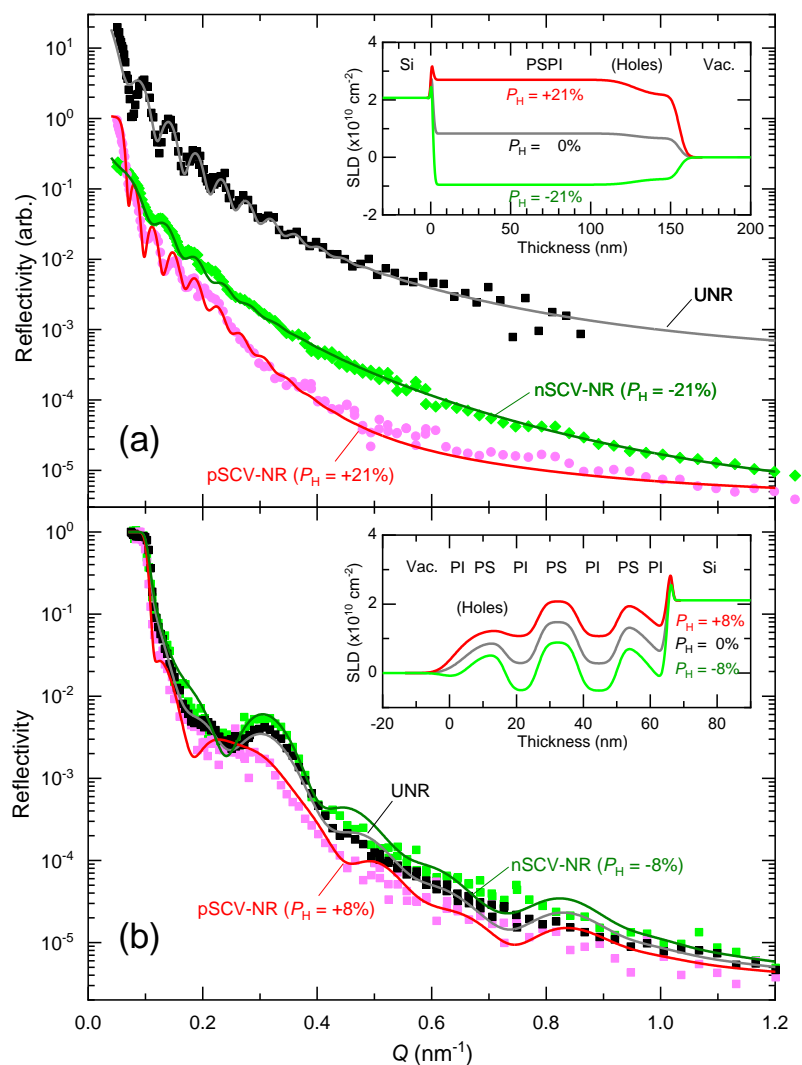


**FIGURE 4.** Same experimental data as in Figure 3, but simulated using the hole model with the SLD profiles in the inset and the parameters in Tables S4 and S5.

## Acknowledgments

We are grateful to Dr. B. van den Brandt and Dr. P. Haulte of Paul Scherrer Institute, Prof. N. Horikawa of Nagoya University, Prof. H. Yayama of Kyushu University, and Prof. M. Motokawa of Osaka University for their fruitful comments and suggestions on developing the proton-polarization apparatus. We also thank Dr. R. Motokawa of JAEA for reading this

manuscript, and Dr. H. Terakado and Ms. A. Konno of JAEA for help us with the optical microscopy measurements. Samples were prepared at the User Experiment Preparation Lab III that is provided by CROSS. Neutron reflectivity measurements were conducted on Proposal No. 2016C0002, 2016I0017, 2017A0062, and 2017B0048 in J-PARC MLF.

### Funding Information

This work was supported in part by the Ministry of Education, Culture, Sports, Science and Technology, Japan (Grant-in-Aid for Scientific Research C, No. 15K04706, 18K11926).

### References

- Abragam, A. & Goldman, M. (1978). *Rep. Prog. Phys.* **41**, 395–467.
- Abragam, A. (1961). *Principles of nuclear magnetism*, Oxford: Clarendon Press.
- Bornet, A. & Jannin, S. (2016). *J. Magn. Reson.* **264**, 13–21.
- Brandrup, J., Immergut, E. H. & Grulke, E. A. (1999). *Polymer handbook, 4th ed.* New York: Wiley-interscience.
- van den Brandt, B., Glättli, H., Grillo, I., Hautle, P., Jouve, H., Kohlbrecher, J., Konter, J. A., Leymarie, E., Mango, S., May, R. P., Stuhmann, H. B. & Zimmer, O. (2002). *Europhys. Lett.* **59**, 62–67.
- van den Brandt, B., Glättli, H., Grillo, I., Hautle, P., Jouve, H., Kohlbrecher, J., Konter, A., Leymarie, E., Mango, S., May, R. P., Michels, A., Stuhmann, H. B. & Zimmer, O. (2006). *Europhys. J. B* **49**, 157–165.
- Coulon, G., Ausserre, D. & Russell, T. P. (1990). *J. de Phys.* **51**, 777–786.
- Crowley, T. L., Lee, E. M., Simister, E. A. & Thomas, R. K. (1991a). *Physica B* **173**, 143–156.
- Crowley, T. L., Lee, E. M., Simister, E. A., Thomas R. K., Penfold, J. & Rennie, A. R. (1991b). *Colloids Surf.* **52**, 85–106.
- Fermon, C., Glättli, H., van der Grinten, M., Eisenkremer, M. & Pinot, M. (1992). *Physica B* **180-181**, 991–992.
- Hamley, I. W. (1998). *The physics of block copolymers*, pp. 221–277. Oxford: Oxford University Press.
- Hartwig, G. (1994). *Polymer properties at room and cryogenic temperatures*, New York: Plenum Press.
- Hasegawa, H. & Hashimoto, T. (1985). *Macromolecules* **18**, 589–590.

Hayashida, H., Takeda, M., Yamazaki, D., Maruyama, R., Soyama, K., Kubota, M., Mizusawa, T., Yoshida, N. & Sakaguchi, Y. (2013). *Phys. Procedia* **42**, 130–135.

Higgins, J. S. & Benoît, H. C. (1996). *Polymers and neutron scattering*, pp. 342–366. New York: Oxford University Press.

Holt, S. A., Le Brun, A. P., Majkrzak, C. F., McGillivray, D. J., Heinrich, F., Lösche, M. & Lakey, J. H. (2009). *Soft Matter* **5**, 2576–2586.

Imae, T., Kanaya, T., Furusaka, M. & Torikai, N. (2011). *Neutrons in soft matter*, p. 115–145. Hoboken: Wiley & Sons.

Knop, W., Hirai, M., Olah, G., Meerwinck, W., Schink, H.-J., Stuhrman, H. B., Wagner, R., Wenkow-EsSouni, M., Zhao, J., Schärpf, O., Crichton, R. R., Krumpolc, M., Nierhaus, K. H., Niinikoski, T. O. & Rijllart, A. (1991). *Physica B* **174**, 275–290.

Knop, W., Schink, H.-J., Stuhmann, H. B., Wagner, R., Wenkow-Es-Souni, M., Schärpf, O., Krumpolc, M., Niinikoski, T. O., Rieubland, M. & Rijllart, A. (1989). *J. Appl. Cryst.* **22**, 352–362.

Kohgi, M., Ishida, M., Ishikawa, Y., Ishimoto, S., Kanno, Y., Masaike, A., Masuda, Y. & Morimoto, K. (1987). *J. Phys. Soc. Jpn.* **56**, 2681–2688.

Kumada, T., Akutsu, K., Ohishi, K., Morikawa, T., Kawamura, Y., Sahara, M., Suzuki, J. & Torikai, N. (2018). *JPS Conf. Proc.* **22**, 011015.

Kumada, T., Noda, Y. & Ishikawa, N. (2012). *J. Magn. Reson.* **218**, 59–65.

Kumada, T., Noda, Y., Hashimoto, T. & Koizumi, S. (2009). *Nucl. Inst. Meth. A* **606**, 669–674.

Kumada, T., Noda, Y., Hashimoto, T. & Koizumi, S. (2010). *J. Chem. Phys.* **133**, 54504.

Liu, D., Wang, T. & Keddie J. L. (2009). *Langmuir* **25**, 4526–4534.

Majkrzak, C. F. & Berk, N. F. (1999). *Physica B* **267-268**, 168–174.

Mutter, R. & Stühn, B. (1995). *Macromolecules* **28**, 5022–5028.

Mutter, R., Strobl, G. & Stühn, B. (1993). *Fresenius J. Anal. Chem.* **346**, 297–299.

Nelson, A. (2006). *J. Appl. Cryst.* **39**, 273–276.

Noda, Y., Koizumi, S., Masui, T., Mashita, R., Kishimoto, H., Yamaguchi, D., Kumada, T., Takata, S., Ohishi, K. & Suzuki, J. (2016) *J. Appl. Cryst.* **49**, 2036–2045.

Noda, Y., Kumada, T., Hashimoto, T. & Koizumi, S. (2011). *J. Appl. Cryst.* **44**, 503–513.

Roe, R. J. (2000). *Methods of X-ray and neutron scattering in polymer science*, pp. 236–260. New York: Oxford Press.

Sears, V. F. (1992). *Neutron News* **3(3)**, 26–37.

Takeda, M., Yamazaki, D., Soyama, K., Maruyama, R., Hayashida, H., Asaoka, H., Yamazaki, T., Kubota, M., Aizawa, K., Arai, M., Inamura, Y., Ito, T., Kaneko, K., Nakamura, T., Nakatani, T., Oikawa, K., Ohara, T., Sakaguchi, Y., Sakasai, K., Shinohara, T., Suzuki, J., Suzuya, K., Tamura, I., To, K., Yamagishi, H., Yoshida, N. & Hirano, T. (2012). *Chi. J. Phys.* **50**, 161–170.

Wenckeback, T. (2016). *Essentials of dynamic nuclear polarization*, Burgh-Haamstede: Spindrift.

## Supporting information

### S1. Analytical derivation of $P_H$ from $Q_c$ and oscillation

The neutrons reflected from the free surface and the interface of a monolayer film with refraction index  $n_f$  interfere at the following conditions,

$$2n_f d \sin \theta_f = N\lambda, \quad (\text{S1})$$

$$2n_f d \sin \theta_f = (N - 1/2)\lambda, \quad (\text{S2})$$

with

$$n_f^2 = 1 - \lambda^2 \rho_f / \pi, \quad (\text{S3})$$

where  $d$  is the film thickness and  $N$  is the natural number. According to the Snell's law, the refraction angle  $\theta_f$  of the neutrons in the film is related to the incident angle  $\theta$ ,

$$n_f \cos \theta_f = \cos \theta. \quad (\text{S4})$$

$Q$  at the minima of the oscillation,  $Q_{\min}$ , is derived from Equations (S1), (S3), and (S4) for  $\rho_f > \rho_{Si}$  or  $\rho_f < 0$  as follows,

$$Q_{\min} = \frac{2\pi}{d} \sqrt{N^2 + \frac{4d^2 \rho_f}{\pi}}, \quad (\text{S5})$$

but that for  $0 < \rho_f < \rho_{Si}$  is given by the Equations (S2)–(S4),

$$Q_{\min} = \frac{2\pi}{d} \sqrt{\left(N - \frac{1}{2}\right)^2 + \frac{4d^2 \rho_f}{\pi}}. \quad (\text{S6})$$

$Q_c$  is obtained by substituting  $\theta_f = 0$  into Equations (2), (S3), and (S4),

$$Q_c = 4\sqrt{\pi \rho_f}, \quad (\text{S7})$$

for  $\rho_f \geq \rho_{Si}$ , and

$$Q_c = 4\sqrt{\pi \rho_{Si}}, \quad (\text{S8})$$

for  $\rho_f < \rho_{Si}$ . Figure S3(a) shows  $Q_{\min}$  and  $Q_c$  of the NR curves of the PS film in Figure 2, which are calculated by substituting  $\rho_f = \rho_{PS}$  and  $d = 77$  nm into Equations (S5)–(S8). Consistently with the MOTOFIT simulation,  $|P_H| = 15 \pm 6\%$  is determined from the intersection in  $Q_{\min}$  and

$Q_c$  between the SCV-NR curves and the calculated values. The interval of  $Q_{\min}$ , which corresponds to the oscillation period, decreases with increasing  $P_H$  according to the decrease in  $\theta_f$  because of Snell's law.

Figure S3(b) shows  $Q_{\min}$  and  $Q_c$  of the NR curves of the strongly annealed PSPI film in Figure 3(a), which are calculated by substituting  $d = 156$  nm and  $\rho_f = \rho_{\text{PSPI}}$  in

$$Q_{\min} = \frac{2\pi}{d} \sqrt{N^2 + \frac{4d^2(\rho_f - \rho_{\text{Si}})}{\pi}}, \quad (\text{S9})$$

for  $\rho_f > \rho_{\text{Si}}$  or  $\rho_f < 0$ ,

$$Q_{\min} = \frac{2\pi}{d} \sqrt{\left(N - \frac{1}{2}\right)^2 + \frac{4d^2(\rho_f - \rho_{\text{Si}})}{\pi}}. \quad (\text{S10})$$

for  $0 < \rho_f < \rho_{\text{Si}}$ , and

$$Q_c = 4\sqrt{\pi(\rho_f - \rho_{\text{Si}})}. \quad (\text{S11})$$

Here,  $\rho_f$  in Equations (S5)–(S7) is replaced by  $\rho_f - \rho_{\text{Si}}$  in Equations (S9)–(S11), respectively, because the neutron beams were irradiated from the rear (Si) side. Consistent with the MOTOFIT simulation,  $|P_H| = 21 \pm 2\%$  is determined from the intersection in  $Q_{\min}$  and  $Q_c$  between the SCV-NR curves and the calculated values.

## S2. MOTOFIT simulation of the hole model

As shown in the microscopy image in Figure S4, the PSPI film has holes whose diameter is ~

1  $\mu\text{m}$  and their depth is close to one period of the lamellar microdomains of  $\sim 20$  nm. Therefore, as shown in Figure S5(a), Mutter *et al.* (1993), and Mutter & Stühn (1995), most of the incident neutrons with the incident angle  $\theta = 0.2^\circ$ – $1.5^\circ$  pass through the free surface of the film before being reflected at the bottom of the hole. Therefore, each neutron reflected from the hole interferes with that from the free surface. To simulate the interference using the MOTOFIT program, we used the double flat-surface model in Figure S5(b). In this model, the SLD below the depth of the holes is  $\rho_f$ , but that above the depth is  $(1 - c)\rho_f$ , where  $c$  is the areal ratio of the holes on the free surface.

**Table S1:** Thickness, SLD, and surface and interface roughness used for the MOTOFIT simulation of the PS film in Figure 2.

	Thickness (nm)	SLD ( $\times 10^{10} \text{ cm}^{-2}$ )			Roughness (nm)
		UNR	pSCV-NR ( $P_H = +16\%$ )	nSCV-NR ( $P_H = -16\%$ )	
Vacuum	-	0			-
PS	77	1.48	2.67	0.29	1.2
SiO	1.36	3.47			1.1
Si	-	2.07			0.5

**Table S2:** Thickness, SLD, and surface and interface roughness used for the MOTOFIT simulation of the strongly annealed PSPI film in Figure 3(a).

	Thickness (nm)	SLD ( $\times 10^{10} \text{ cm}^{-2}$ )			Roughness (nm)
		UNR	pSCV-NR ( $P_H = +21\%$ )	nSCV-NR ( $P_H = -21\%$ )	
Si	-	2.07			-
SiO	1.36	3.47			0.5
PSPI	156	0.83	2.70	-0.95	1.0
Vacuum	-	0			4.0

**Table S3:** Thickness, SLD, and surface and interface roughness used for the MOTOFIT simulation of the weakly annealed PSPI film in Figure 3(b).

	Thickness (nm)	SLD ( $\times 10^{10} \text{ cm}^{-2}$ )			Roughness (nm)
		UNR	pSCV-NR ( $P_H = +8\%$ )	nSCV-NR ( $P_H = -8\%$ )	
Vacuum	-	0			-
PI	4.46	0.28	1.07	-0.51	3.93
PS	9.07	1.48	2.08	0.89	3.61
PI	10.66	0.28	1.07	-0.51	3.89
PS	11.96	1.48	2.08	0.89	2.12
PI	11.36	0.28	1.07	-0.51	2.10
PS	9.05	1.48	2.08	0.89	2.64
PI	5.79	0.28	1.07	-0.51	4.97
SiO	1.36	3.47			1.11
Si	-	2.07			0.5

**Table S4:** Thickness, SLD, and surface and interface roughness used for the MOTOFIT simulation of the strongly-annealed PSPI film in Figure 4(a).

	Thickness (nm)	SLD ( $\times 10^{10} \text{ cm}^{-2}$ )			Roughness (nm)
		UNR	pSCV-NR ( $P_H = +21\%$ )	nSCV-NR ( $P_H = -21\%$ )	
Si	-	2.07			-
SiO	1.36	3.47			0.5
PSPI	126	0.83	2.70	-0.95	1.0
PSPI with 20% hole	28	0.66	2.16	-0.76	10
Vacuum	-	0			3.5

**Table S5:** Thickness, SLD, and surface and interface roughness used for the MOTOFIT simulation of the weakly annealed PSPI film in Figure 4(b).

	Thickness (nm)	SLD ( $\times 10^{10} \text{ cm}^{-2}$ )			Roughness (nm)
		UNR	pSCV-NR ( $P_H = +8\%$ )	nSCV-NR ( $P_H = -8\%$ )	
Vacuum	-	0			-
PI with 40% hole	4.46	0.17	0.64	-0.31	3.95
PS with 40% hole	9.07	0.89	1.25	0.53	3.02
PI	10.66	0.28	1.07	-0.51	3.90
PS	11.96	1.48	2.08	0.89	2.01
PI	11.36	0.28	1.07	-0.51	2.49
PS	9.05	1.48	2.08	0.89	4.95
PI	5.79	0.28	1.07	-0.51	2.69
SiO	1.36	3.47			1.10
Si	-	2.07			0.5

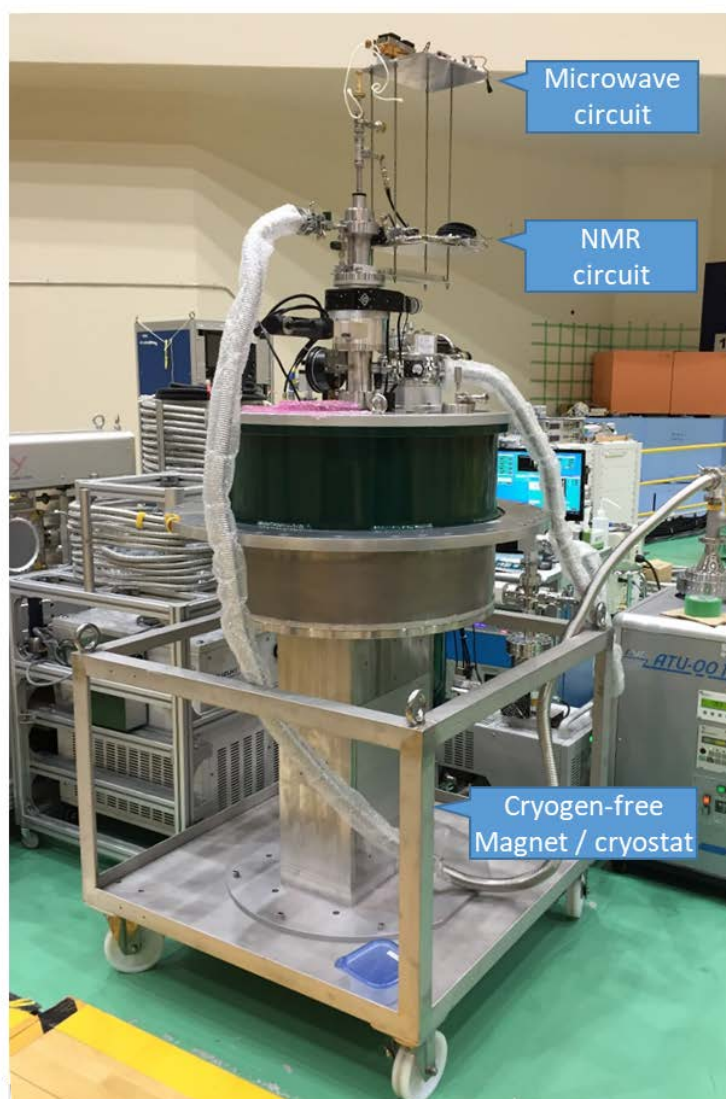


**Figure S1:** DNP apparatus.

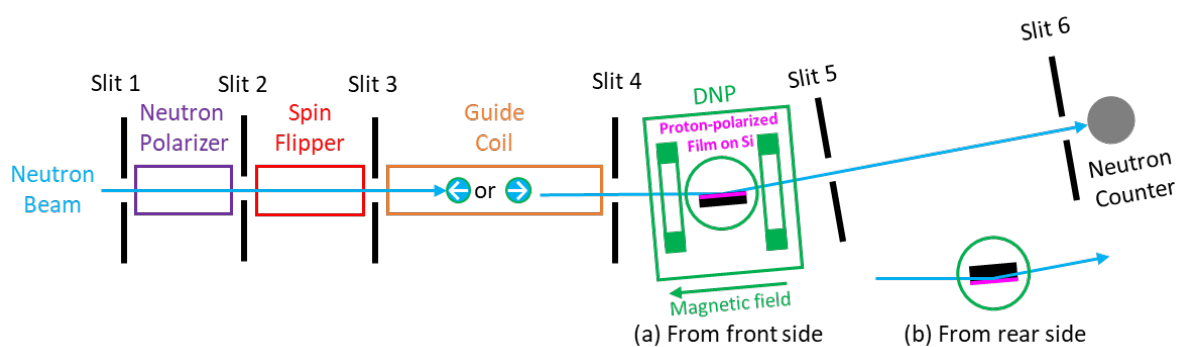


**Figure S2:** Layout of the SCV-NR measurement.

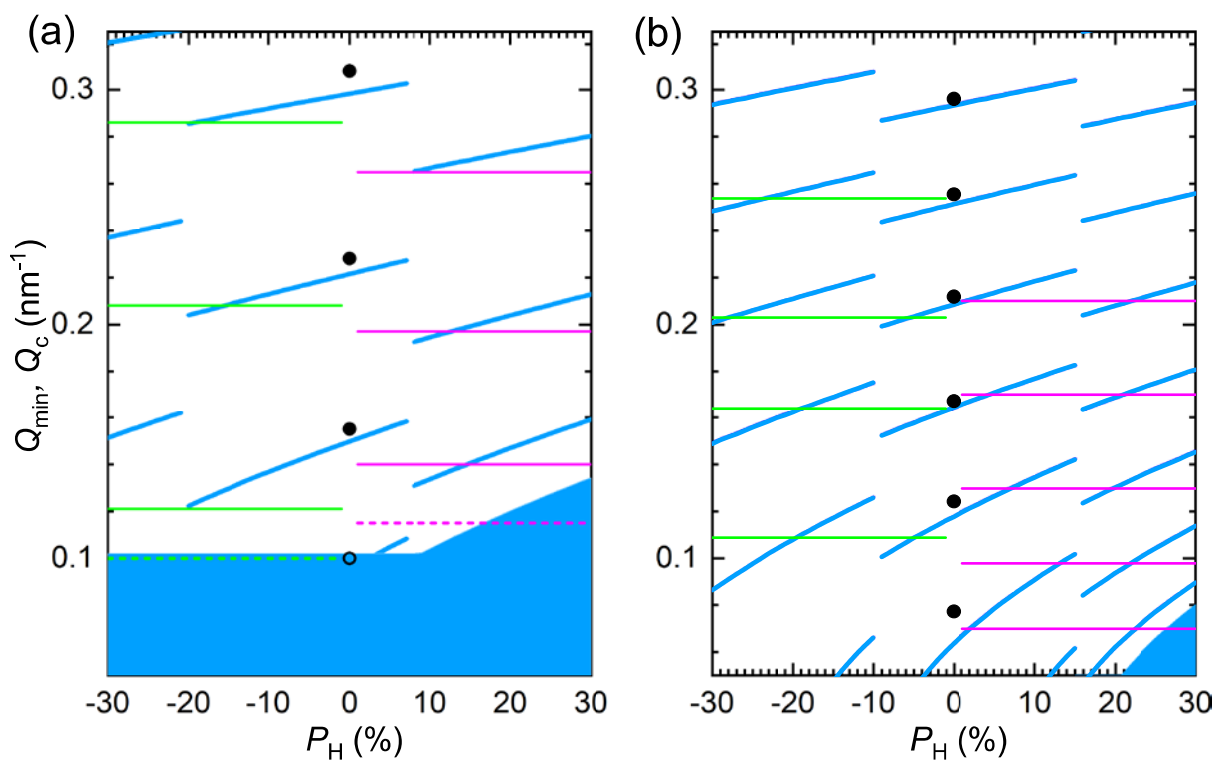


**Figure S3:**  $Q_{\min}$  (solid) and  $Q_c$  (dashed) of (a) the PS film in Figure 2 (green) and (b) the strongly annealed PSPI film in Figure 3(a) (magenta). Blue bold lines,  $Q_{\min}$  calculated by substituting  $d = 77$  nm in Equations (S5) and (S6) in (a) and 155 nm in Equations (S9) and (S10) in (b); boundary with blue filled area,  $Q_c$  from Equations (S7) and (S8) in (a) and Equation (S11) in (b); closed and open circles,  $Q_{\min}$  and  $Q_c$  of the UNR curve, respectively.

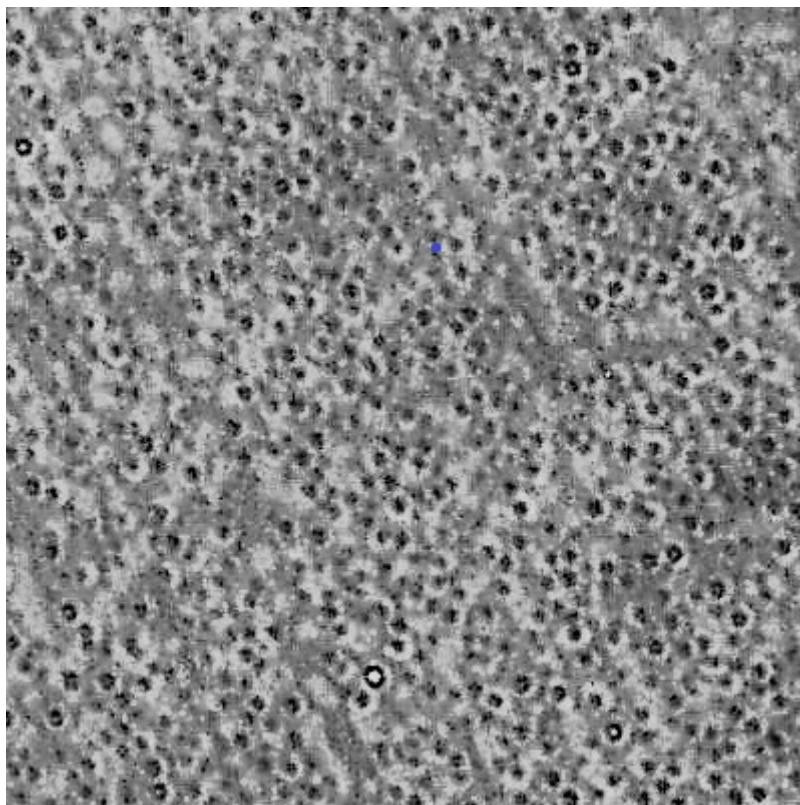


**Figure S4:** Optical microscopy image of the weakly annealed PSPI film using Keyence VHX-500. Length of a side is 80  $\mu\text{m}$ . According to the results of X-ray reflectivity by Mutter et al. (1993) and Mutter and Stühn (1995), the micrometer-sized black dots are attributed to the holes.

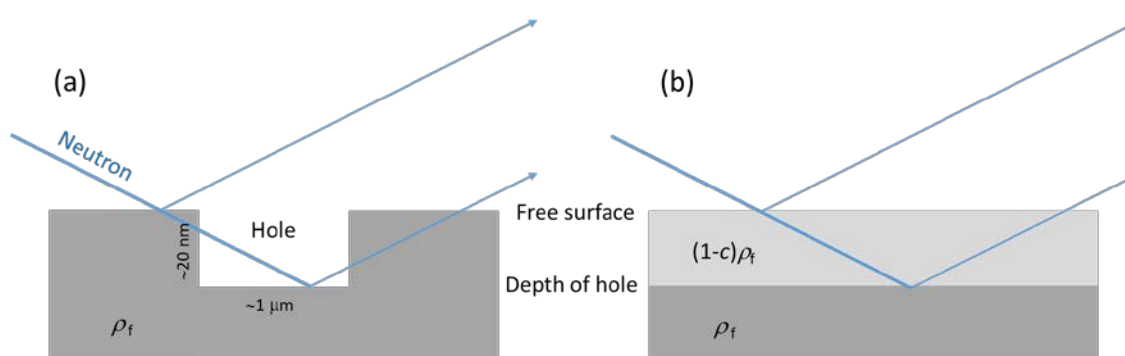


**Figure S5:** Superposition of neutrons reflected at the free surfaces and bottom of the holes. According to Mutter and Stühn (1995), the double flat-surface model (b), which has a flat layer with a depth of the hole and SLD of  $(1-c)\rho_f$ , is used to simulate reflections from the surface having holes with the areal occupation ratio  $c$  (a).